

Applying 2DEG in High-Performance Mid-Infrared Photodetection

Hanlun Xu, Yao Wang, Jinbo Shen, Ziyang Ren, Jiaqi Zhu, Yansong Chen, Mengjuan Liu, Yihui Zhai, Yunhao Lu, Yong Zhang, Shiyao Zhu, Sihan Zhao,* and Huizhen Wu*

High-speed and highly sensitive infrared photodetectors are regarded as one of the most essential components in modern photonic devices and technology because of constantly emerging application scenarios. In this paper, an ultrafast and extremely low noise mid-infrared (MIR) photodetector is reported at both room and cryogenic temperatures by leveraging the high-mobility 2D electron gas (2DEG) at the polar CdTe/PbTe heterostructure interface. The detector simultaneously exhibits a peak detectivity of $\approx 4.2 \times 10^{11}$ Jones with rapid response in the order of 10 ns, which is substantially superior to the state-of-the-art 2DEG MIR detectors made of 2D layered materials. The ultrafast response with extremely low noise of the 2DEG photodetector is attributed to the unique band alignment at the interface. The practical infrared imaging application is further showcased using the 2DEG MIR detector by revealing the fine features of a MIR radiation target. This work highlights the promising prospect of utilizing the unique 2DEG interface in the field of high-speed and highly sensitive MIR detection.

photodetector is one of the most essential components in such detection systems. 2D electron gas (2DEG) has constantly shown a plethora of cornerstone discoveries in condensed matter physics in the past few decades,^[7–13] in which the high-mobility carrier motion confined within the 2D interface makes it distinct from other condensed matter systems. These peculiar findings at 2D interfaces have provided alternative and intriguing avenues to explore innovative applications in photodetection. Some salient examples include the high-performance ultraviolet photodetector based on AlGaIn/GaN,^[14] visible photodetector based on MgZnO/ZnO,^[15] long-wavelength infrared photodetector based on AlGaAs/GaAs,^[16–18] etc. Although these 2DEG systems have been exploited in detecting photons with different energies, the reports of 2DEG in detecting MIR photons are rare.

The emergence of 2D layered materials unlocked the possibility of detecting MIR photons utilizing 2DEG for carriers in 2D layered materials are naturally confined within the 2D surfaces, which is forming 2DEG. A wide range choice of 2D layered materials with appropriate bandgaps results in an extensive application in MIR detection, alongside with the recent develop-

1. Introduction

Photodetection with higher sensitivity and faster speed in mid-infrared (MIR) spectral range (3–5 μm) serves as a pivotal force to the advances of modern technology in numerous emerging fields such as aerospace, environmental protection, fire warning, food and medical care, autonomous driving, etc.^[1–6] A MIR

H. Xu, Y. Wang, J. Shen, Z. Ren, Y. Chen, M. Liu, Y. Zhai, Y. Lu, S. Zhu, S. Zhao, H. Wu
School of Physics and Zhejiang Province Key Laboratory of Quantum Technology and Device
Zhejiang University
Hangzhou, Zhejiang 310058, China
E-mail: sihanzhao88@zju.edu.cn; hzwu@zju.edu.cn
H. Xu, Y. Wang, J. Shen, Z. Ren, Y. Chen, M. Liu, Y. Zhai, Y. Lu, S. Zhao, H. Wu
State Key Laboratory for Silicon and Advanced Semiconductor Materials
Zhejiang University
Hangzhou, Zhejiang 310058, China
H. Xu, Y. Wang, Z. Ren, Y. Chen, M. Liu, Y. Zhai, S. Zhu, S. Zhao, H. Wu
Interdisciplinary Center for Quantum Information
Zhejiang University
Hangzhou, Zhejiang 310058, China

J. Zhu
Hangzhou Institute for Advanced Study
University of Chinese Academy of Sciences
Hangzhou, Zhejiang 310024, China
Y. Zhang
Department of Electrical and Computer Engineering
The University of North Carolina at Charlotte
Charlotte, NC 28223, USA
S. Zhu
Hefei National Laboratory
Hefei, Anhui 230088, China
H. Wu
Research Center for Sensing Materials and Devices
Zhejiang Lab
Hangzhou, Zhejiang 311121, China

 The ORCID identification number(s) for the author(s) of this article can be found under <https://doi.org/10.1002/adom.202300602>

DOI: 10.1002/adom.202300602

ment of sample stacking technique.^[19,20] For example, a broad-band detection was achieved by PtTe₂, PtSe₂, WS₂, graphene, and their heterostructures.^[21–24] Moreover, high operation temperature was also realized by black arsenic phosphorus or black phosphorus detectors in MIR detection in comparison with conventional narrow bandgap semiconductors such as HgCdTe or InSb.^[25–28] In spite of the progress made using 2D layered materials and their heterostructures in MIR photodetectors, a delicate balance among fast response speed, high responsivity, and low noise level, which is required for a high-performance MIR detector, remains an outstanding challenge. For example, most of the photodetectors using 2D layered materials (including black phosphorus) fail in the rapid photodetection of MIR light, due to the low response speed although the responsivity remains high with a depressed noise level.^[21–28] Even for the claimed rapid photodetectors made of 2D PtTe₂, the reported response time falls in the order of a few μs .^[21] Another impediment for widespread application of 2D layered materials in MIR detection is the instability in ambient environment, which entails sophisticated sample protection procedure throughout the fabrications and measurements.^[19,29] Furthermore, mono- or few-layered 2D materials cannot offer sufficient MIR absorption for most general-purpose applications, because each monolayer can only achieve a few percent optical absorbance.

CdTe/PbTe is an extraordinary heterostructure with 2DEG spontaneously formed at the interface without intentional doping.^[30,31] Owing to the unique energy band alignment of CdTe/PbTe heterostructure,^[30,31] only the high-mobility 2D electrons at the interface contribute to the photoresponse signals of the MIR detector, as revealed by the previous works.^[32,33] In this article, we report a rapid and highly sensitive 2DEG MIR photodetector, in which electrons are confined at the epitaxial CdTe/PbTe (111) interface with high mobility. In contrast to the weak absorption of 2D layered materials, a 3 μm thick PbTe is used for photosensitive layer, permitting a sufficient light absorption. The detector simultaneously achieves ultrafast speed (in the order of ≈ 10 ns) and high detectivity ($\approx 4.2 \times 10^{11}$ Jones) in detecting MIR photons, outperforming almost all the 2DEG MIR detectors made of 2D layered materials.^[21,23,25,27,34] Even comparing to the traditional MIR HgCdTe detectors, we find that our detector is faster not only at room temperature but also at cryogenic temperatures, meanwhile retaining a comparable detectivity.^[35,36] We also systematically analyze the noise spectra in the frequency domain, and assign the noise origin at various frequency range of interest, which is pivot to determining the detector detectivity and understanding the noise characteristics of the 2DEG detector. The combined theoretical band structure calculation and experimental noise spectra pinpoint the underlying origin of the high-performance of the 2DEG detector in MIR detection, accounting for the unique properties simultaneously achieved in the detector, including ultrafast response, extremely low noise and high sensitivity. MIR imaging of a hot target using the 2DEG detector is further demonstrated at room temperature, revealing fine features without noise spikes. Given the stability of the detector in atmosphere is significantly improved by the presence of CdTe capping layer, a wide variety of applications can be envisioned. Our 2DEG heterostructure thus provides a novel route to fabricating a rapid and stable MIR detector with low operating noise in high-speed and highly sensitive MIR detection.

2. Results and Discussions

2.1. CdTe/PbTe Heterostructure Interface

CdTe/PbTe (111) heterostructure was formed by molecular beam epitaxy (MBE) technique. We employed a freshly cleaved BaF₂ (111) as the growth substrate. First, a PbTe layer with a thickness of ≈ 3 μm was grown on BaF₂ and then immediately followed by the growth of CdTe capping layer with a thickness of ≈ 100 nm. The 2DEG was formed at the interface spontaneously without intentional doping because both CdTe and PbTe are polar in the (111) plane and share compatible hexagonal symmetry. Owing to the close lattice constants of 6.46 and 6.48 \AA at room temperature (RT) respectively, the heterostructure formed by PbTe and CdTe shows very small interfacial lattice mismatch. **Figure 1a** presents an image of cross-sectional high-resolution transmission electron microscopy (HRTEM) that shows the typical CdTe/PbTe (111) interface. Although PbTe and CdTe belong to rocksalt and zinc-blend crystal structures, respectively (**Figure 1b**), an atomically sharp interface with negligible lattice imperfections is observed. Distinct crystal structures can further reduce the mutual atom diffusion between the two crystals. We observe an unusual bonding configuration from **Figure 1a**, that is, CdTe and PbTe share an interfacial Te atomic layer. The interfacial Te atoms will receive excessive valence electrons contributed from Cd atoms and Pb atoms from both CdTe and PbTe sides. It is the excess electrons at the interfacial Te layer that form the 2DEG at the interface and lead to the high electron density with particularly high mobility.^[30,31,37] Band structure calculations of the heterostructure are performed by the density-functional theory (DFT) and the results are shown in **Figure 1c**. It is seen that the bands cross the Fermi level, indicating that the interface is metallic and the 2DEG is formed at the interface. **Figure 1d** depicts the X-ray diffraction (XRD) pattern of the CdTe/PbTe heterostructure on a BaF₂ substrate. All the observed XRD peaks can be assigned to the corresponding (111) and (222) polar crystalline planes, verifying the preferential layer-by-layer growth along [111] direction normal to the BaF₂ substrate. The peaks of CdTe and PbTe partially overlap (inset of **Figure 1d**), confirming the minimal mismatch at the heterostructure interface.

2.2. Photodetector Structure and Characteristics of Infrared Response

Architecture of our photodetector based on the CdTe/PbTe 2DEG interface is schematically depicted in **Figure 2a**. A photovoltaic configuration is employed in the detector. Cu electrodes were deposited at both ends of the 2DEG channel for the readout of photoelectric signals. The channel is typically designed with 600 μm in length and 800 μm in width. The half of the area is covered with a deposited Au film on the top (insulated from the right-side Cu electrode by an insulating layer) which divides the 2DEG channel into two parts with equal area, i.e., the photosensitive region (left part of the channel in **Figure 2a**) and the photoshielded region (right part of the channel in **Figure 2a**). When infrared light impinges on the detector, only the photosensitive region is exposed to the radiation. Since CdTe does not absorb MIR radiation because of its wide bandgap ($E_g = 1.51$ eV), MIR light transmits through CdTe and is absorbed by the narrow bandgap PbTe (E_g

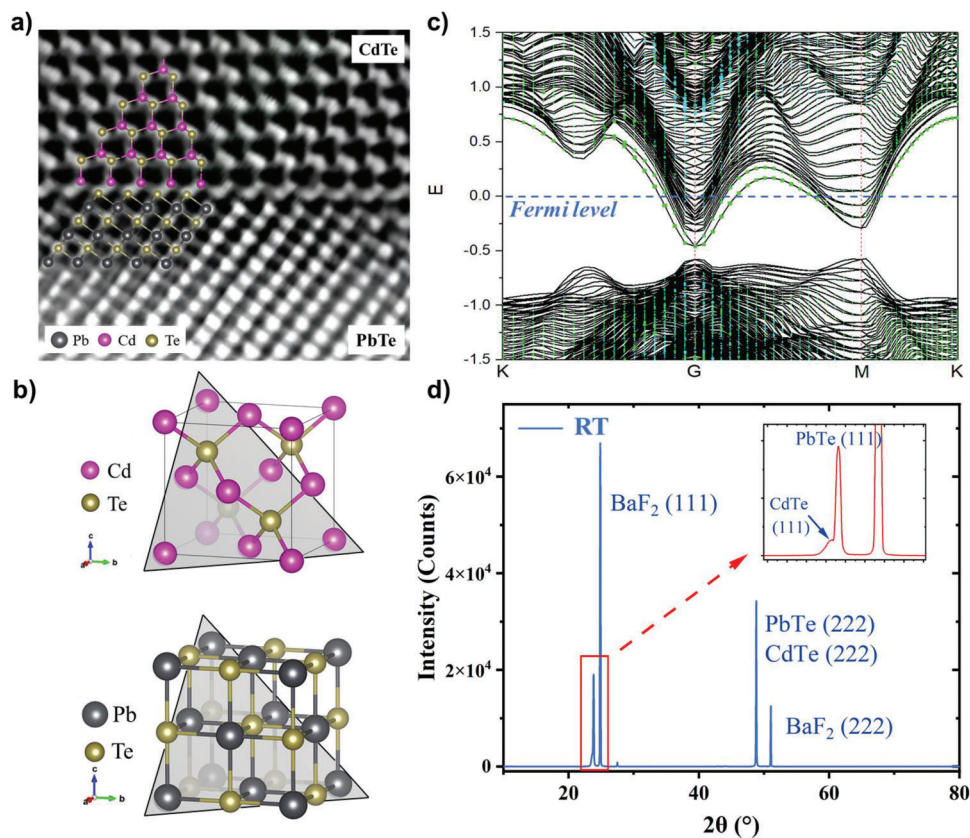


Figure 1. Interface of CdTe/PbTe (111) heterostructure. a) The HRTEM image of a typical CdTe/PbTe (111) interface grown on a BaF₂ substrate (not shown in the image) by MBE. Ball-stick models of PbTe and CdTe crystals, indicating the atomic arrangement, are overlaid on the HRTEM image. An atomically sharp interface with a perfect lattice bonding at the interface is observed. CdTe and PbTe share an interfacial Te atomic layer, which is responsible for the high electron density of the 2DEG at the interface. b) Crystal structures of rock-salt PbTe and zincblende CdTe, where the (111) planes for both crystals are denoted by gray triangles. c) Calculated band structure of CdTe/PbTe (111) heterostructure, where the green dots in the bands are the projection for PbTe at the interface and the cyan dots are the ones for CdTe. The electronic states shown at the Fermi level (indicated by a blue dashed line) suggest a metallic interface where 2DEG is formed. d) The XRD pattern of the CdTe/PbTe heterostructure. The data are measured in the reflection configuration with Cu K α radiation at RT. The diffraction peaks are assigned to different indices of the crystalline planes as shown in (d). Note that the partial overlap between peaks of PbTe and CdTe (inset of Figure 1d) confirms a minimal lattice mismatch at the heterostructure interface.

= 0.32 eV), producing photogenerated carriers in the PbTe layer. Figure 2b illustrates the calculated energy band diagram at the interface, where the space-resolved densities of states (DOS) are represented by different colors. The Fermi level (E_F) is indicated by the red dashed line, and that the position of CdTe/PbTe interface is marked by the black dashed line. The white lines depict the contours with DOS of 0.5 (in arbitrary units). The appreciable DOS at the interface at E_F clearly shows the accumulation of free electrons at the interface, giving rise to the metallic 2DEG. Interestingly, due to the large valence band offset (VBO) between CdTe and PbTe shown in Figure 2b, nearly all the photogenerated holes are blocked and retain in the PbTe layer, whereas, on the other hand, the photogenerated electrons are able to quickly relax into the 2DEG channel due to the band bending at the CdTe/PbTe interface (Figure 2b). As a result, the electron density in the channel underneath the photosensitive region is higher than that of the photoshielded region, leading to an asymmetric distribution of electric charges (and the Fermi levels as well) along the 2DEG channel. As such, an electric field parallel to the heterostructure interface is created and a potential difference will be generated

across the two Cu leads,^[33] which allows the detector to operate under zero bias (i.e., the photovoltaic mode). Our 2DEG MIR detector operates in a similar manner as the detectors made of 2D layered materials for the transport channels of the photogenerated carriers are confined within a 2D plane in both cases, while the 3 μ m thick PbTe layer underneath 2DEG in our case can result in much more efficient absorption of incident MIR photons than those for 2D layered materials.

Figure 2c shows the spectral response of the detector at RT. The cut-off wavelength represents the absorption edge above which the detector does not offer significant response to the radiation, and is defined as the corresponding wavelength at which the photoelectric response reaches 50% of the peak value. The cut-off wavelength of $\approx 4 \mu$ m is obtained at RT, which is indicated by the black dashed line. The MIR photocurrent response at lower temperatures down to 88 K is further shown in Figure S1a–d in the Supporting Information. We observe the cut-off wavelength redshift with decreasing temperature, which is consistent with the unusual bandgap shrinkage of the PbTe layer with lowering temperature^[38] (Figure S1e, Supporting

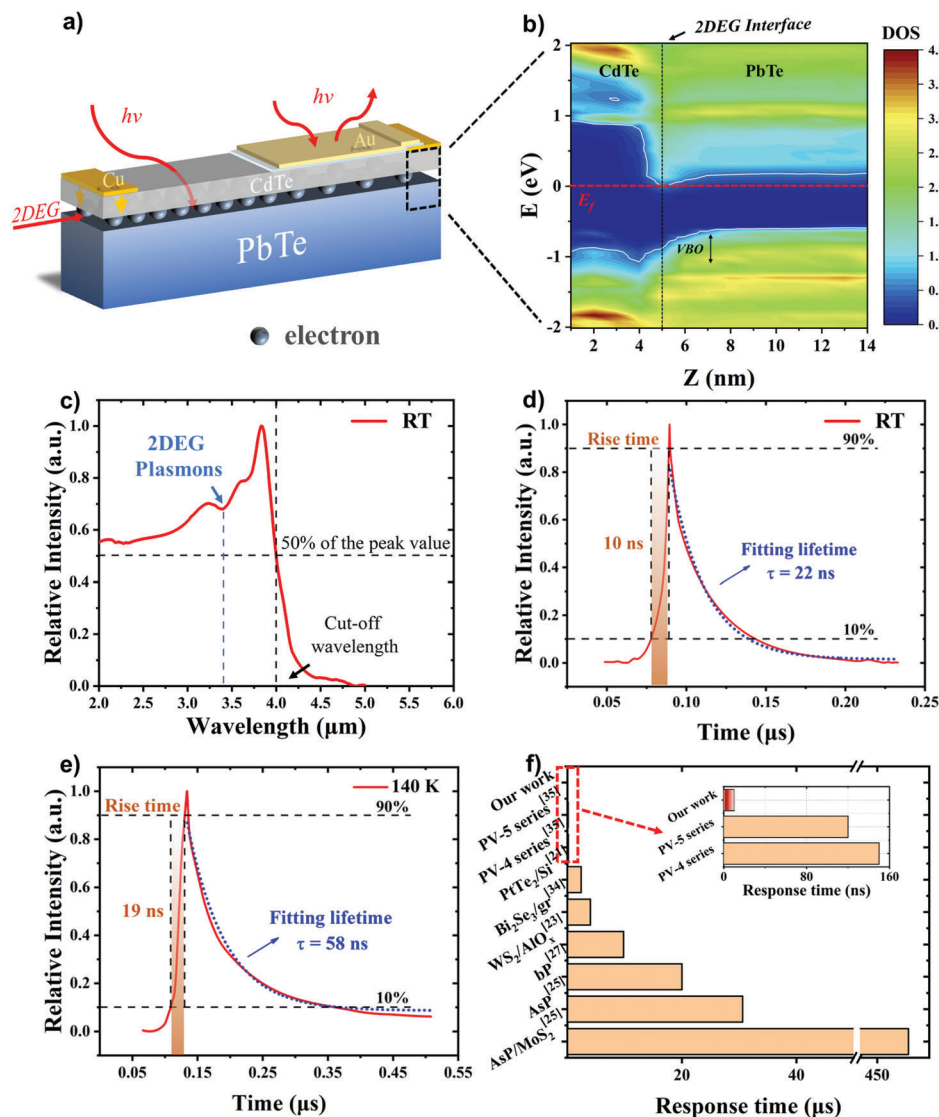


Figure 2. Detector structure and the MIR response. a) Architecture of the detector based on the CdTe/PbTe interface 2DEG. Cu films deposited on the two ends of the channel are used as electrodes, and the Au film working as the light shielded layer divides the 2DEG channel into two equal parts to obtain the asymmetric MIR exposure. Note that the Au film is insulated from the right-side Cu electrode by an insulating layer (see the Experimental Section for the detail). b) Calculated space-resolved DOS of the CdTe/PbTe (111) heterostructure. The Fermi level (E_f) is indicated by the red dashed line, and that the position of CdTe/PbTe interface is marked by the black dashed line. The white lines depict the contours with DOS of 0.5 (in arbitrary units). The appreciable DOS at the interface at E_f clearly shows the accumulation of free electrons at the interface, giving rise to the metallic 2DEG. Because of the large VBO, the photogenerated carriers (i.e., electrons) by MIR light transit and relax into the 2DEG channel, whereas, on the other hand, the holes are blocked at the interface. c) The MIR photoelectric response spectrum of the detector measured at RT. The cut-off wavelength of $\approx 4 \mu\text{m}$ (indicated by the black dashed line) is defined as the wavelength at which the photoelectric response reaches 50% of the peak value of the first response peak above the PbTe absorption edge. A dip at $\approx 3.4 \mu\text{m}$ is attributed to the light absorption caused by the 2DEG localized plasmons (indicated by the blue arrow). d,e) Transient photoelectric response of the detector measured at RT and 140 K with the excitation wavelength of $\approx 2.5 \mu\text{m}$, respectively. The pulse laser duration time is ≈ 220 fs with a repetition rate of ≈ 100 kHz. The rise time of the photoelectric response is also labeled, which is chosen as the time segments from 10% to 90% of the peak response (shaded regions). The fitting results of the carrier lifetime are displayed by the dotted blue line. f) Comparison of response time for our detector and state-of-the-art detectors working in MIR based on 2D layered materials and their heterostructures. The response time of MIR HgCdTe pin detectors (PV-5 series and PV-4 series) provided by VIGO is also presented in the figure. The inset is the enlarged view showing the response time of our detector. Note that the time unit of the inset is in ns, indicating the response speed of our detector is about three orders faster than those of the detectors based on the 2D layered materials and their heterostructures. Compared with the advanced HgCdTe pin detectors, response time of our detector still shows advantage.

Information). Therefore, we can conclude that the photogenerated carriers and photocurrent response of our detector are predominantly contributed from PbTe, being consistent with the band diagram proposed in Figure 2b.

Although our detector employs a lateral device structure (like a photoconductive detector), the photogenerated electron relaxation path from the PbTe layer to the 2DEG interface is extremely short, similar to the vertically stacked heterostructures composed of 2D layered materials.^[21,39] Furthermore, the high mobility of 2DEG at the CdTe/PbTe interface yields a rapid photoresponse, which is much superior to those of the 2D layered heterostructures.^[21,27,34,40,41]

The transient photoelectric response measured at two representative temperatures is shown in Figure 2d,e with ≈ 2.5 μm laser pulse excitation. Measurements at some other cryogenic temperatures and other two excitation wavelengths in the response spectrum of our detector are shown in Figures S2a–d and S3 (Supporting Information), respectively. We chose the time segments from 10% to 90% of the peak response as the rise time (shaded regions in Figure 2d,e) upon the pulse radiation.^[42] The rise time measured at RT yields ≈ 10 ns (Figure 2d). We note that the photogenerated electron relaxation time into 2DEG channel is in fact ultrafast, taking place on the order of ≈ 100 fs.^[43] The observed rise time is still limited by the approx GHz bandwidth of our instrumentation used in the experiment. The maximum rise time is observed at 120–140 K, and it still yields a rise time shorter than 20 ns, suggesting that the detector retains its rapid photoresponse at low temperatures. Figure 2f compares the high-speed response (rise time) of our 2DEG detector with the state-of-the-art MIR detectors made from 2D layered materials and their heterostructures. It is clear that the response time of our 2DEG detector is 3–5 orders of magnitude shorter than those of the detectors made from 2D layered materials.

We further use a single exponential function to fit the fall dynamics to extract the carrier lifetime as displayed by the blue dotted lines in the Figure 2d,e. The carrier lifetime of our detector first increases with cooling from RT. It reaches a maximum value at 140 K with a carrier lifetime of ≈ 58 ns (Figure 2e). When temperature decreases further from 140 K, the lifetime decreases again, giving rise to ≈ 25 ns at 77 K (Figure S2e, Supporting Information). The increase of carrier lifetime from RT to 140 K is because the majority carriers which are holes in PbTe decreases with cooling,^[44] making the recombination rate between photogenerated electrons (minority carriers) and holes smaller and therefore a longer lifetime of the electrons. The downturn of lifetime below 140 K is presumably due to the structural faults of PbTe crystals at the low temperature, which is discussed in Figure S4 in the Supporting Information.

2.3. High-Performance in Mid-Infrared Photodetection with Low Noise

Responsivity, which characterizes the conversion efficiency of a photodetector from light to electrical power, is one of the key metrics to evaluate the detector performance. Because of the bandgap shrinkage of the PbTe layer with decreasing temperature (Figure S1a–d, Supporting Information), we use peak response values

around the absorption edge to represent the responsivity of our detector at varying temperatures. The data are shown by the red circles in Figure 3a. The peak responsivity at RT is ≈ 63 mA W^{-1} at wavelength of ≈ 4 μm . Responsivity rapidly increases as the temperature decreases from 230 to 140 K, and reaches its maximum at 120 K at wavelength of ≈ 5 μm . The peak responsivity is ≈ 3.26 A W^{-1} at 120 K, more than 50 times higher than that at RT. Longer lifetime of carriers in PbTe at low temperatures indicates more photogenerated electrons can relax down to the 2DEG channel, thus more charges can be collected by Cu electrodes. This will lead to the increase of responsivity. When the operating temperature is lower than 120 K, the responsivity starts to show a gradual decrease. Interestingly, peak responsivity and the carrier lifetime exhibit similar temperature dependence and their maximum values emerge at close temperatures (≈ 140 K) (Figure 3a; Figure S2e, Supporting Information). We also calculate the external quantum efficiency (EQE) of the 2DEG detector, which is shown in Figure S5 in the Supporting Information. The maximum EQE of our detector reaches 80% at ≈ 140 K. There are two primary reasons for the high EQE of the 2DEG detector. First, the high EQE of our detector benefits from the large absorption coefficient of PbTe^[44] together with a thick photon-absorption layer (≈ 3 μm). Second, only photogenerated electrons can relax to the 2DEG channel from PbTe layer and transport in the 2DEG channel due to the large valence band offset at the interface, leading to a small generation and recombination rates (Figure 2b).

Noise investigation is crucial to evaluate the performance of a MIR photodetector. In general, the measured noise of a detector is the superposition of $1/f$ noise, generation–recombination ($g-r$) noise, white noise, etc.^[45] Here, we examine the noise characteristics of our 2DEG detector in the frequency domain from 1.0 Hz to 1.4 kHz at RT. The data are shown in Figure 3b, where $1/f$ noise, $g-r$ noise, white noise and the overall fitting result are denoted by the blue, green, purple dashed lines and the black solid line, respectively (see the Experimental Section). We observe that for $f < 20$ Hz, the noise power density is inversely proportional to the frequency, suggesting that the detector is primarily limited by the $1/f$ noise at low frequency;^[46] for 20 $\text{Hz} < f < 100$ Hz, the noise current mainly originates from the $g-r$ noise for the data can be fitted by a single Lorenz function;^[47] for $f > 100$ Hz, noise power density remains constant regardless of the frequency, signifying the dominant role of white noise beyond 100 Hz. The characteristic frequency at which the noise spectrum reaches the onset of the white noise is defined as the corner frequency f_0 (blue arrow in Figure 3b), which serves as an important figure of merit for a detector.^[45] Generally, white noise represents for the lowest noise level of a detector,^[45] so that the lower corner frequency is, the lower noise will the detector have in low frequency. In this case, lower chopping rate can be used for the operation of a MIR detector, which leads to broad and practical applications. The corner frequency f_0 of our detector is determined to be ≈ 100 Hz, which is orders of magnitude smaller than those of detectors made from 2D layered materials such as high-mobility graphene (> 5000 Hz)^[45] or conventional MIR HgCdTe pin detectors.^[48,49] The obtained time constant τ associated with trapping states is ≈ 734 μs for 20 $\text{Hz} < f < 100$ Hz where the $g-r$ noise dominates. The larger τ is, the less is the influence of the $g-r$ noise exerting on the low frequency noise, which leads to a lower

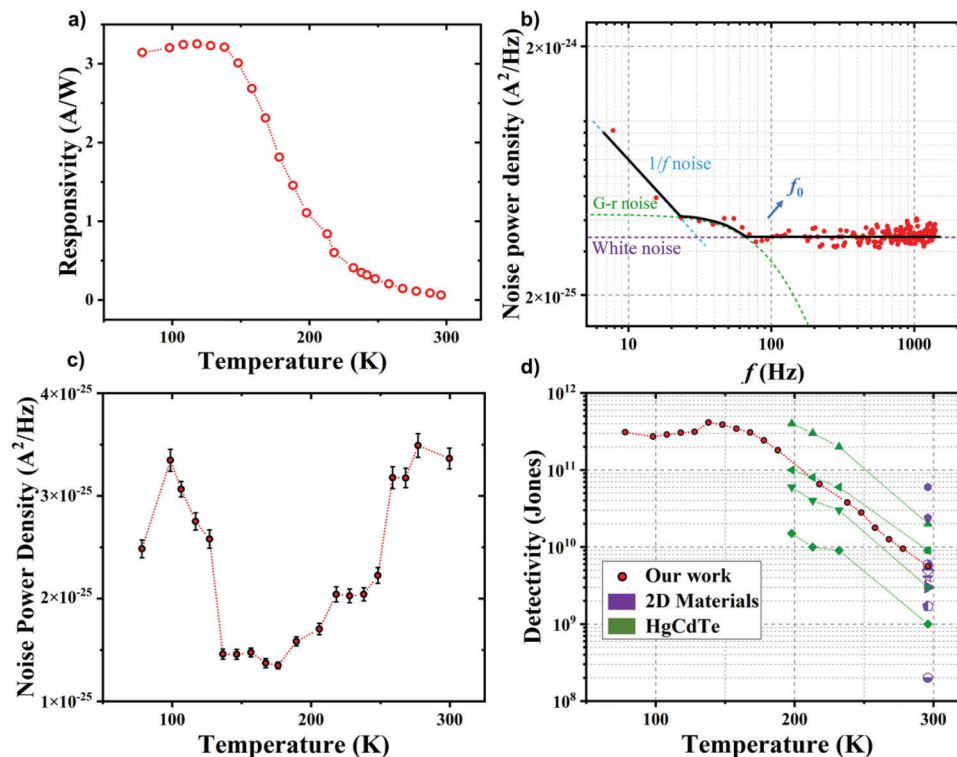


Figure 3. Responsivity, noise and detectivity of the 2DEG photodetector. a) Peak responsivity of our detector measured from RT to 77 K. b) Noise power density measured at RT, where the $1/f$ noise, $g-r$ noise, white noise and the overall fitting result are denoted by the blue, green, purple dashed lines and the black solid line, respectively. A corner frequency of ≈ 100 Hz is indicated by the blue arrow, demonstrating a diminutive noise level at low frequency. c) Amplitude of white noise power density from RT to 77 K. We take the root mean square (RMS) value of the white noise power density for frequency from 1.0 to 1.4 kHz. The error bars are defined as the root mean square error (RMSE) value of the corresponding data. d) Peak detectivities of our detector from RT to 77 K. The detectivities of MIR HgCdTe pin detectors and 2D layered material detectors working at $\lambda \approx 4 \mu\text{m}$ are also shown for comparison. Data of this work are denoted by the red circles. Detectivities of the reported detectors made from 2D layered materials are displayed by purple tags, with \bullet for the black phosphorus photoconductive detector proposed by Kim et al.,^[27] \circ for the black phosphorus photoconductive detector proposed by Amani et al.,^[28] \blacklozenge for the black arsenic phosphorus photoconductive detector,^[28] \blacktriangleleft for the black arsenic phosphorus/MoS₂ heterostructure,^[25] \blackstar for the PtTe₂/Si heterostructure,^[21] \blacktriangleright for the WS₂/AlO_x/Ge heterostructure,^[23] \blacklozenge for the Bi₂Se₃/graphene heterostructure,^[34] and \bullet for the black arsenic phosphorus FET,^[25] respectively. Detectivities for the MIR HgCdTe pin detectors are denoted by the green tags, with \blacksquare for Thorlabs VL5T0,^[36] and \blacktriangledown , \blacktriangle , \blacklozenge and \blacktriangleleft for VIGO PV-4 series, PVI-4 series, PV-5 series, and PVI-5 series, respectively.^[35]

corner frequency f_0 . Given the large VBO at the CdTe/PbTe interface (Figure 2b), holes could barely relax into the 2DEG channel, so that the fluctuation of generation and recombination rates of electrons in the 2DEG channel is very small. Hence, our detector exhibits a large time constant of $g-r$ noise and a remarkably small corner frequency f_0 . Our 2DEG detector also displays ultralow white noise with noise power density S_n of $\approx 3 \times 10^{-25} \text{ A}^2 \text{ Hz}^{-1}$ at RT. The low noise feature of our 2DEG detector is mainly attributed to the unique band alignment of the CdTe/PbTe interface (Figure 2b) where the photogenerated electrons can directly relax from PbTe into the 2DEG channel in close vicinity without passing through any potential barrier. White noise of our 2DEG detector operated at different temperatures is shown in Figure 3c. Due to the less thermal perturbation at low temperatures, the white noise gets smaller and smaller when cooling down. However, it increases rapidly with further cooling below 140 K. Combined with the measured responsivity in Figure 3a and white noise power density in Figure 3c, we can obtain the

specific detectivities of our detector at different temperatures by using the following equation

$$D^* = \frac{R\sqrt{A_d}}{\sqrt{S_n}} \quad (1)$$

where R , A_d , and S_n stand for the responsivity, the area of photo-sensitive region and the white noise power density, respectively. The obtained detectivities as a function of temperature are presented in Figure 3d. With $A_d = 300 \times 800 \mu\text{m}^2$, the detector has a detectivity of $\approx 5.6 \times 10^9$ Jones at wavelength of $\approx 4 \mu\text{m}$ at RT. The detectivity sharply increases with the decrease of temperature. The maximum detectivity reaches $\approx 4.2 \times 10^{11}$ Jones at 140 K at wavelength of $\approx 4.8 \mu\text{m}$. Detectivities of the high-performance MIR detectors made from 2D layered materials^[21,23,25,27,34] are shown in Figure 3d for comparison. Our 2DEG detector achieves a detectivity that is higher than most of the MIR detectors based on 2D layered materials.

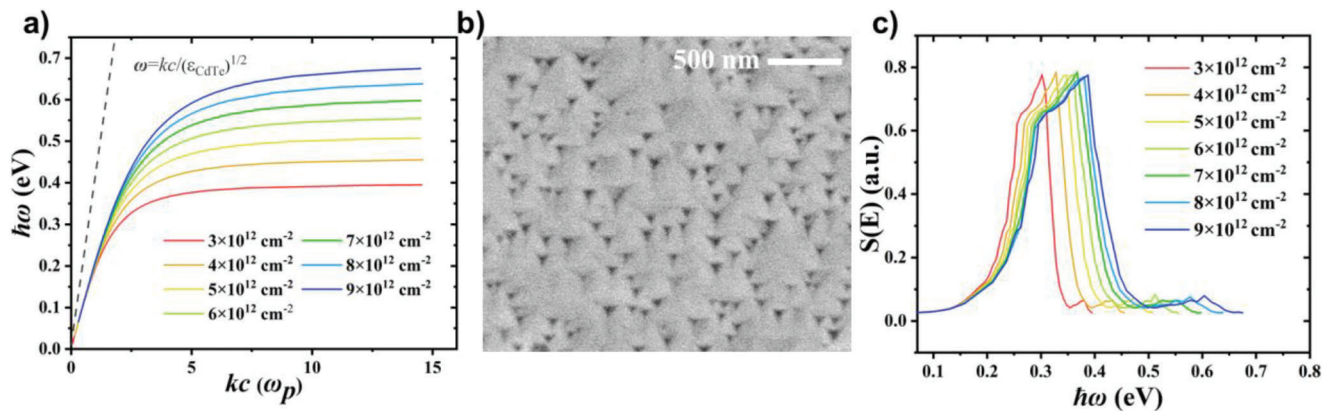


Figure 4. 2DEG localized plasmons at the CdTe/PbTe interface. a) Calculated results for the dispersion relation of the perfect interface plasmons as a function of electron concentrations ranging from 3×10^{12} to $9 \times 10^{12} \text{ cm}^{-2}$. The dispersion relation of incident light in CdTe is shown by the gray dashed line, where the momentum mismatch between the perfect interface plasmons and incident light is expected. b) Scanning electron microscopy (SEM) image of the triangular pits on the surface of epitaxial PbTe with a CdTe capping layer of $\approx 100 \text{ nm}$. The scale bar on the top right is 500 nm. c) Structure factor as a function of photon energy calculated for the same range of electron concentrations as in (a). The energies of the $S(E)$ peaks evolve from 0.34 to 0.38 eV, which is consistent with the observed photoelectric response dips in Figure 2c and Figure S1a–d in the Supporting Information.

We would like to note here that HgCdTe as a conventional material system is widely used in MIR detection as well. Our 2DEG detector exhibits a much shorter response time both at room temperature and low temperatures while remaining a comparable detectivity performance in comparison with the advanced commercial MIR HgCdTe pin photodiodes (Figures 2f and 3d; Figure S6 and Table S1, Supporting Information). As for MIR HgCdTe avalanche photodiodes (APDs) that have ultrafast photoresponse and ultrahigh detectivity due to the high gain coming from the carrier multiplication,^[50–52] we believe they are the competitive candidates mainly at low temperatures.^[53] HgCdTe APDs usually need to operate with supplying relatively high bias voltages, and they exhibit relatively high noise at high temperatures,^[54] while our 2DEG photovoltaic detector has advantages of lower power consumption, lower noise and ultrafast speed at both room and low temperatures.

It is noted that the MIR responsivity (Figure 3a), carrier lifetime (Figure S2e, Supporting Information) and white noise power density (Figure 3c) deteriorate at low temperatures below 140 K, showing responsivity saturation, decrease in lifetime and increase in noise power density, respectively. Temperature-dependent XRD was used to explore the underlying degradation mechanism of CdTe/PbTe epitaxial samples at low temperatures. A representative XRD pattern of CdTe/PbTe at the temperature of 138 K is shown in Figure S4a in the Supporting Information. Figure S4b (Supporting Information) summarizes the temperature-dependent peak intensity (red dots) and the corresponding full width at half maximum (FWHM, shown by the black dots) of PbTe (111) extracted from the XRD patterns measured at low temperatures. As temperature decreases below $\approx 130 \text{ K}$, the peak intensity of PbTe (111) reduces, accompanied by an increased FWHM, which indicates an increase of defect density in the PbTe lattice. These changes presumably come from the stress accumulation and relaxation for the thermal expansion coefficient of between PbTe and BaF_2 substrate differ from each other at the low temperature.^[44,55]

2.4. 2DEG Localized Plasmons at the CdTe/PbTe Interface

Distinct from the intrinsic photoconductive response of PbTe crystals,^[56] all the response spectra of our 2DEG detector exhibit prominent temperature-independent dips at $3.4 \mu\text{m}$ or 0.36 eV (Figure 2c; Figure S1a–d, Supporting Information). This dip (indicated by the blue arrow in Figure 2c) can be attributed to the excitation of the localized plasmons at the 2DEG interface comprised of high concentration electrons. It is the excited localized plasmons that lead to reduced optical absorption of the underneath PbTe layer that generates photocurrent. To confirm this, we first calculated the dispersion relation of interface plasmons as a function of electron concentrations as shown in Figure 4a, where ω_p , k , and c is plasmon frequency, wave vector, and the speed of light, respectively. The calculation details are given in the Supporting Information. However, the interface plasmons cannot be excited by the incident free-space photons due to the apparent momentum mismatch since the plasmon dispersion curves reside outside the light cone (grey dashed line in Figure 4a). The formation of randomly distributed triangular pits on the surface of PbTe (111) has been observed (Figure 4b), which could provide the additional momentum through scattering in the plasmon excitation.^[57,58] We can obtain the structure factor $S(k)$, which characterizes the scattering probability distribution by the triangular pits defined in the reciprocal space.^[59] Combined with the calculated plasmon dispersion in Figure 4a, we can then obtain the structure factor $S(E)$ as a function of energy at different electron concentrations. The results are given in Figure 4c, showing clearly the resonant excitation of localized plasmons, enabled by the triangular pits, with varying peak energy at different electron concentrations. For 2DEG with a sheet electron density in the range of $5 \times 10^{12} - 9 \times 10^{12} \text{ cm}^{-2}$, $S(E)$ assumes the peak value between 0.34 and 0.38 eV, meaning that the infrared photons in this range are most efficiently scattered by the triangular pits. This is consistent with the observed photocurrent dips in Figure 2c and Figure S1a–d in the Supporting Information. The triangular

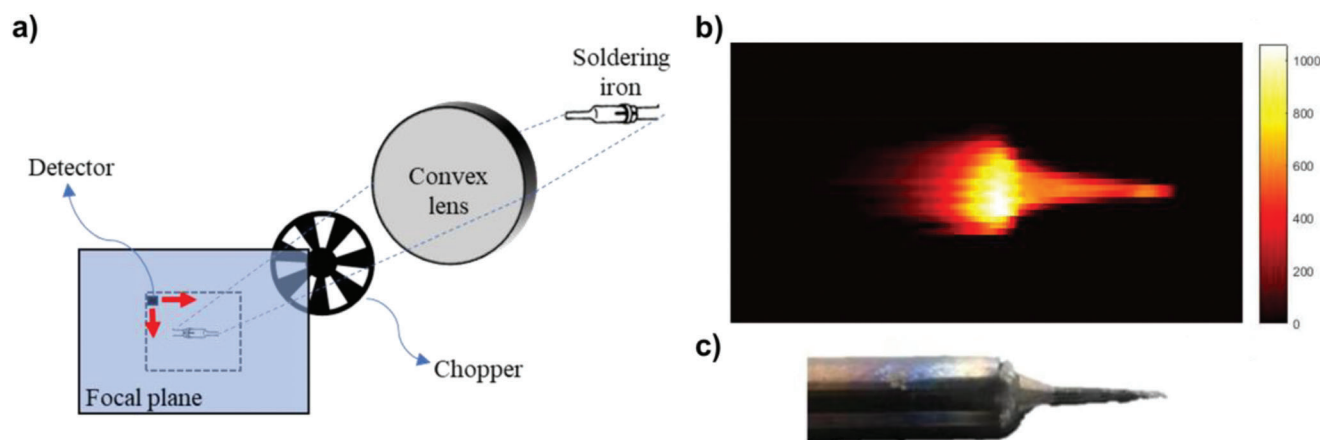


Figure 5. Imaging of a hot target at RT using the 2DEG detector. a) Schematic of the imaging experiment. The MIR radiation from a hot soldering iron is focused by a MIR-compatible convex lens. The detector mounted on a stepper motor is placed at the focal plane of the lens. With the step motor scanning within the focal plane (gray dashed frame), we can form the 2D MIR radiation image of the whole soldering iron with a mechanical chopper. b) Imaging result of a hot soldering iron (≈ 600 K) by our 2DEG detector. Importantly, we can clearly visualize the shape of the solder tip with smooth edges and without noise speckles outside the tip. A mechanical chopper operating at ≈ 400 Hz is used for obtaining the imaging result, at which only the white noise affects the detector performance (see Figure 3b). c) A photograph of the same soldering iron.

pits in the CdTe/PbTe heterostructure cause undesirable photoresponse of the 2DEG detectors, which can be potentially improved by fine tuning of the growth parameters during epitaxy.

2.5. MIR Imaging of A Hot Target

The practical application of using our CdTe/PbTe 2DEG detector operating at RT is demonstrated by imaging a hot soldering iron (≈ 600 K). The measuring scheme is shown in Figure 5a. A MIR-compatible convex lens (50 mm focal length) is used to converge the infrared radiation from the hot soldering iron onto the lens' focal plane where we place our 2DEG detector. The detected signal is measured using a lock-in technique modulated at 400 Hz with a mechanical chopper. Note that at this frequency, only white noise affects the performance of our detector. By using a motor-driving mechanism to scan the detector across the focus plane, we obtain the 2D MIR radiation image of the whole soldering iron. The representative imaging result is shown in Figure 5b. We can clearly visualize the shape of the solder tip with smooth edges and without noise speckles outside the tip. The resolution of MIR imaging can be greatly improved by developing a 2D array of CdTe/PbTe 2DEG photodetectors. Given that the high-quality wafer-scale CdTe/PbTe heterostructure samples can be grown on silicon wafer by making use of BaF₂ or CaF₂ as a buffer layer,^[60–62] it is promising to achieve high-quality and high-speed real-time imaging by exploiting silicon integrated circuits for the signal readout of the 2D array of 2DEG photodetectors.

3. Conclusion

In conclusion, we have developed a novel MIR detector with extremely high speed, low noise and highly sensitive detectivity in comparison with the state-of-the-art MIR detectors exploiting the

interface 2DEG originated from the unique band alignment of CdTe/PbTe heterostructure. Benefited from the ultrafast relaxation of the electrons to the 2DEG channel, the upper bound of the response time of our detector is ≈ 10 ns at RT and ≈ 20 ns at 140 K, which is at least three orders in magnitude faster than the detectors made of 2D layered materials and their heterostructures. Both the unique band alignment and the carrier transport behavior of our 2DEG detectors offer ultralow $1/f$ noise and $g-r$ noise as well as a very low corner frequency f_0 of only ≈ 100 Hz, which is substantially smaller than those of 2D layered material-based detectors and HgCdTe detectors reported so far. We combined the theoretical calculation of band structures and experimental noise spectra to pinpoint the underlying origin of the low-noise level of our 2DEG detector. The combined experimental and theoretical results unambiguously demonstrated the very low corner frequency is mainly attributed to the unique band structure, that is, the large VBO at the CdTe/PbTe interface. The photogenerated electrons rapidly relax from PbTe layer into the 2DEG channel in close vicinity without passing through any potential barrier, accounting for the very low noise properties of our detector. The maximum detectivity is as high as $\approx 5.6 \times 10^9$ Jones at RT, and $\approx 4.2 \times 10^{11}$ Jones at 140 K. The detector remains its rapid response when operation temperature cools down. The overall performances of our 2DEG detector are significantly superior to most of the 2D layered material detectors. Finally, demonstration of a high-quality MIR imaging for a hot target using our 2DEG detector is given. In this regard, given that the high-quality wafer-scale CdTe/PbTe heterostructure samples can be grown on silicon wafer by making use of BaF₂ or CaF₂ as a buffer layer,^[60–62] it is promising to achieve high-quality and real-time imaging by exploiting silicon integrated circuits for the signal readout of the 2D array of 2DEG photodetectors in the future. Our work unlocks the promising and tremendous prospect of leveraging 2DEG in heterostructures in the field of high-performance MIR detection.

4. Experimental Section

Details of the DFT Calculation: The calculations were based on the DFT and implemented by the Vienna ab initio simulation package (VASP).^[63] The generalized gradient approximation (GGA) parametrized by Perdew–Burke–Ernzerhof (PBE)^[64] was used for exchange–correlation potential. The primitive cells of PbTe and CdTe were optimized first and the lattice constants of them are well matched. In order to achieve the interface structure while reducing the nonphysical electrical field, the surfaces were “cleaved” of PbTe and CdTe with [111] direction, choosing 64 layers of PbTe to simulate the substrate, along with 24 layers of CdTe to construct the interface. In addition, a vacuum layer above 20 Å in the Z direction was used to avoid the effect of periodicity. CdTe and PbTe shared an interfacial Te atomic layer. The pseudo-hydrogen atoms were used to saturate dangling bonds on the upper and lower surfaces. Since the system contains heavy elements such as Pb and Te, the spin-orbit coupling (SOC) was considered in the self-consistent and band calculations. During the calculation, the atomic positions were fully relaxed until the residual force per atom was less than 0.02 eV Å⁻¹. In this case, the K-point meshes within the Monkhorst–Pack scheme were selected as 5 × 5 × 1.^[65] After the optimization, the interlayer spacing of PbTe (111) near the interface changed from equal spacing to alternating wide and narrow, while the interlayer spacing of CdTe (111) did not change much.

Fabrication Process of the Device: CdTe/PbTe (111) heterostructure was epitaxially grown on a BaF₂ substrate by an MBE system. PbTe layer with a thickness of 3 μm was selected because of its large absorption coefficient.^[44] Deep UV lithography was used followed by ICP etching to define the 2DEG channel, which was 600 μm in length and 800 μm in width. Then 10 nm thick Cr and 100 nm thick Cu were deposited on both ends by magnetron sputtering. In order to perform Ohmic contact between the Cu electrodes and the 2DEG channel, the as-made sample was heating to 150 °C for 10 min. Under this circumstance, Cu atoms diffused through the CdTe capping layer, and contacted with 2DEG directly. As such, the photogenerated electrons at CdTe/PbTe interface were collected by the Cu electrodes. A 150 nm thick Au film was used to construct the shielded layer covering the half of the channel surface through deep UV lithography and magnetron sputtering. To prevent possible short-circuiting, the shielded layer was isolated from the Cu electrodes through an insulating polymer, which is SU8 in this case. The device structure of the detector was shown in Figure 2a and the photo of the device was presented in Figure S1f in the Supporting Information.

Measurement Systems for Photoelectric Characters of the Detector: Measurements for photoelectric characteristics were performed as follows. The schematics are shown in Figure S7 in the Supporting Information.

Infrared response spectra—A spectroscopy measurement system was used to measure infrared response spectra of the fabricated detector, which was composed of a blackbody source (SiC), a chopper (SRS SR540), a grating monochromator (Zolix Omni-λ 300), a current preamplifier (SRS SR570), and a lock-in amplifier (SRS SR830). The detector operated in a top-incidence mode, that is, infrared light was incident from the CdTe side.

Noise power density—Noise characteristics were measured using a system consisting of a JC-PB2001 electromagnetic shielding box, a FEMTO DLPCA-100 preamplifier and an SRS SR770 spectrum analyzer. During the measurement, the detector was placed inside the shielding box to prevent the interference of electromagnetic waves of the environment.

Transient photoelectric response—A dynamic characterization system was used consisting of a high speed current preamplifier (FEMTO DHPCA-100), an oscilloscope (Tektronix TBS1052B), a wavelength-tunable pulsed laser made up of an fs-pulsed laser (Yb:KGW) and an optical parametric amplifier (OPA, ORPHEUS-ONE) to measure the response time of the detector at different wavelengths. In order to obtain the performance data of the detector at different temperatures, the measurements were performed with the detector sealed in a Dewar, which was cooled by liquid nitrogen.

Noise Analysis: The noise of a detector can be categorized into 1/f noise, g–r noise, white noise, etc. 1/f noise comes from the random fluctuation of the carriers, which can be modeled by Lorentz function with characteristic time constants that are associated with certain types of trap states.^[45] If there is no dominant trap state in a detector, the total noise

can be expressed as a superposition of the composite perturbations with different time constants, which is linear correlated with frequency. This type of noise is defined as 1/f noise. Usually, 1/f noise takes the form of $S = kI^b/f^a$, where S is noise power density, I is the current flowing through the detector; a , b , k are the parameters related to frequency, current, and device fabrication process, respectively. If there are dominant trap states in the detector, bulges with defined time constants are superimposed on the total noise power density. These bulges are manifested as protrusion in the Lorentzian function of the noise spectra and defined as the g–r noise. In a photodetector, time constant (τ) can be obtained by fitting the g–r noise using Lorenz function

$$S_l(f) = \frac{S_0}{[1 + (2\pi f\tau)^2]} \quad (2)$$

where S_0 is the noise power density with frequency $f \ll (2\pi\tau)^{-1}$, τ is the time constant associated with trapping states. The larger τ is, the less is the influence of the g–r noise exerting on the low frequency noise. A large time constant of $\tau \approx 734 \mu\text{s}$ is obtained for the detector which explains the small corner frequency of $\approx 100 \text{ Hz}$.

Supporting Information

Supporting Information is available from the Wiley Online Library or from the author.

Acknowledgements

The authors acknowledge the Micro-Nano Processing Platform, Institute of Microelectronics and Nanoelectronics, Zhejiang University for the fabrication of the devices. The authors thank Prof. Haiming Zhu from the Department of Chemistry, Zhejiang University, for providing the measurement system of transient photoelectric response. This work was mainly supported by the National Key R&D Program of China (2019YFE0112000), Zhejiang Provincial Natural Science Foundation of China (LR21A040001), National Natural Science Foundation of China (11933006), and Sino-German Center for Science (GZ 1580). S.Z. was supported by the National Key R&D Program of China (2022YFA1203400) & Zhejiang Provincial Natural Science Foundation of China (LR23A040002). S.Z. was also supported by the National Natural Science Foundation of China (12174335) and ZJU 100 Talents Program of Zhejiang University. S.Z. thanks the Innovation Program for Quantum Science and Technology (grant no. 2021ZD0303200).

Conflict of Interest

The authors declare no conflict of interest.

Data Availability Statement

The data that support the findings of this study are available from the corresponding author upon reasonable request.

Keywords

2DEG, mid-infrared photodetectors, noise analysis, ultrafast photoreponse

Received: March 12, 2023
Revised: April 24, 2023
Published online:

- [1] T. J. Dupuy, A. L. Kraus, *Science* **2013**, *341*, 1492.
- [2] R. Soref, *Nat. Photonics* **2010**, *4*, 495.
- [3] A. Schliesser, N. Picqué, T. W. Hänsch, *Nat. Photonics* **2012**, *6*, 440.
- [4] S. S. Kumar, J. Hult, J. Picotte, B. Peterson, *Remote Sens.* **2020**, *12*, 238.
- [5] R. H. Wilson, H. S. Tapp, *TrAC, Trends Anal. Chem.* **1999**, *18*, 85.
- [6] X. Lu, H. M. Al-Qadiri, M. Lin, B. A. Rasco, *Food Bioprocess Technol.* **2011**, *4*, 919.
- [7] K. v. Klitzing, G. Dorda, M. Pepper, *Phys. Rev. Lett.* **1980**, *45*, 494.
- [8] D. C. Tsui, H. L. Stormer, A. C. Gossard, *Phys. Rev. Lett.* **1982**, *48*, 1559.
- [9] M. Konig, S. Wiedmann, C. Brune, A. Roth, H. Buhmann, L. W. Molenkamp, X.-L. Qi, S.-C. Zhang, *Science* **2007**, *318*, 766.
- [10] N. Reyren, S. Thiel, A. D. Caviglia, L. F. Kourkoutis, G. Hammerl, C. Richter, C. W. Schneider, T. Kopp, A.-S. Ruetschi, D. Jaccard, M. Gabay, D. A. Muller, J.-M. Triscone, J. Mannhart, *Science* **2007**, *317*, 1196.
- [11] Y. Kozuka, M. Kim, C. Bell, B. G. Kim, Y. Hikita, H. Y. Hwang, *Nature* **2009**, *462*, 487.
- [12] Y. Cao, V. Fatemi, S. Fang, K. Watanabe, T. Taniguchi, E. Kaxiras, P. Jarillo-Herrero, *Nature* **2018**, *556*, 43.
- [13] G. Scalari, C. Maissen, D. Turcinkova, D. Hagenmuller, S. De Liberato, C. Ciuti, C. Reichl, D. Schuh, W. Wegscheider, M. Beck, J. Faist, *Science* **2012**, *335*, 1323.
- [14] Y.-Y. Zhang, Y.-X. Zheng, J.-Y. Lai, J.-H. Seo, K. H. Lee, C. S. Tan, S. An, S.-H. Shin, B. Son, M. Kim, *ACS Nano* **2021**, *15*, 8386.
- [15] J. D. Hwang, C. C. Yang, C. M. Chu, *ACS Appl. Mater. Interfaces* **2017**, *9*, 23904.
- [16] Z. F. Paska, J. Y. Andersson, L. Lundqvist, C.-O. A. Olsson, *J. Cryst. Growth* **1991**, *107*, 845.
- [17] J. Chu, S. S. Li, P. Ho, *Appl. Phys. Lett.* **1996**, *69*, 1258.
- [18] O. O. Cellek, J. L. Reno, Y.-H. Zhang, *Appl. Phys. Lett.* **2012**, *100*, 241103.
- [19] M. Long, P. Wang, H. Fang, W. Hu, *Adv. Funct. Mater.* **2019**, *29*, 1803807.
- [20] T. Tan, X. Jiang, C. Wang, B. Yao, H. Zhang, *Adv. Sci.* **2020**, *7*, 2000058.
- [21] L. Zeng, D. Wu, J. Jie, X. Ren, X. Hu, S. P. Lau, Y. Chai, Y. H. Tsang, *Adv. Mater.* **2020**, *32*, 2004412.
- [22] X. Yu, P. Yu, D. Wu, B. Singh, Q. Zeng, H. Lin, W. Zhou, J. Lin, K. Suenaga, Z. Liu, Q. J. Wang, *Nat. Commun.* **2018**, *9*, 1545.
- [23] D. Wu, J. Guo, C. Wang, X. Ren, Y. Chen, P. Lin, L. Zeng, Z. Shi, X. J. Li, C.-X. Shan, J. Jie, *ACS Nano* **2021**, *15*, 10119.
- [24] H. Lin, Y. Song, Y. Huang, D. Kita, S. Deckoff-Jones, K. Wang, L. Li, J. Li, H. Zheng, Z. Luo, H. Wang, S. Novak, A. Yadav, C.-C. Huang, R.-J. Shiue, D. Englund, T. Gu, D. Hewak, K. Richardson, J. Kong, J. Hu, *Nat. Photonics* **2017**, *11*, 798.
- [25] M. Long, A. Gao, P. Wang, H. Xia, C. Ott, C. Pan, Y. Fu, E. Liu, X. Chen, W. Lu, T. Nilges, J. Xu, X. Wang, W. Hu, F. Miao, *Sci. Adv.* **2017**, *3*, e1700589.
- [26] M. Buscema, D. J. Groenendijk, S. I. Blanter, G. A. Steele, H. S. J. van der Zant, A. Castellanos-Gomez, *Nano Lett.* **2014**, *14*, 3347.
- [27] H. Kim, S. Z. Uddin, D.-H. Lien, M. Yeh, N. S. Azar, S. Balendhran, T. Kim, N. Gupta, Y. Rho, C. P. Grigoropoulos, K. B. Crozier, A. Javey, *Nature* **2021**, *596*, 232.
- [28] M. Amani, E. Regan, J. Bullock, G. H. Ahn, A. Javey, *ACS Nano* **2017**, *11*, 11724.
- [29] N. R. Glavin, R. Rao, V. Varshney, E. Bianco, A. Apte, A. Roy, E. Ringe, P. M. Ajayan, *Adv. Mater.* **2020**, *32*, 1904302.
- [30] S. Jin, C. Cai, G. Bi, B. Zhang, H. Wu, Y. Zhang, *Phys. Rev. B* **2013**, *87*, 235315.
- [31] B. Zhang, P. Lu, H. Liu, L. Jiao, Z. Ye, M. Jaime, F. F. Balakirev, H. Yuan, H. Wu, W. Pan, Y. Zhang, *Nano Lett.* **2015**, *15*, 4381.
- [32] S. Ma, K. Li, H. Xu, J. Zhu, H. Zhu, H. Wu, *ACS Appl. Mater. Interfaces* **2019**, *11*, 39342.
- [33] J. Zhu, H. Xu, Z. Wang, Y. Chen, S. Ma, N. Ali, H. Zhu, A. Rahimi-Iman, H. Wu, *Optica* **2020**, *7*, 1394.
- [34] J. Kim, S. Park, H. Jang, N. Koirala, J.-B. Lee, U. J. Kim, H.-S. Lee, Y.-G. Roh, H. Lee, S. Sim, S. Cha, C. In, J. Park, J. Lee, M. Noh, J. Moon, M. Salehi, J. Sung, S.-S. Chee, M.-H. Ham, M.-H. Jo, S. Oh, J.-H. Ahn, S. W. Hwang, D. Kim, H. Choi, *ACS Photonics* **2017**, *4*, 482.
- [35] VIGO Photonics S.A., HgCdTe (MCT) Photovoltaic Detectors, <https://vigophotonics.com/products/infrared-detectors/hgcdc-te-mct-photovoltaic-detectors> (accessed: February 2023).
- [36] Thorlabs Inc., Mid-IR Photovoltaic Detectors, HgCdTe (MCT), https://www.thorlabschina.cn/newgroupage9.cfm?objectgroup_id=11319 (accessed: February 2023).
- [37] B. Zhang, C. Cai, H. Zhu, F. Wu, Z. Ye, Y. Chen, R. Li, W. Kong, H. Wu, *Appl. Phys. Lett.* **2014**, *104*, 161601.
- [38] Y. Zhang, X. Ke, P. R. C. Kent, J. Yang, C. Chen, *Phys. Rev. Lett.* **2011**, *107*, 175503.
- [39] K. J. Lee, K. Kwon, S. Kim, W. Hong, J. Park, K. Yu, S.-Y. Choi, *Adv. Opt. Mater.* **2020**, *8*, 1901519.
- [40] S. Zhao, J. Wu, K. Jin, H. Ding, T. Li, C. Wu, N. Pan, X. Wang, *Adv. Funct. Mater.* **2018**, *28*, 1802011.
- [41] F. Wang, Y. Zhang, Y. Gao, P. Luo, J. Su, W. Han, K. Liu, H. Li, T. Zhai, *Small* **2019**, *15*, 1901347.
- [42] R. B. Jacobs-Gedrim, M. Shanmugam, N. Jain, C. A. Durcan, M. T. Murphy, T. M. Murray, R. J. Matyi, R. L. Moore, B. Yu, *ACS Nano* **2014**, *8*, 514.
- [43] G. Perraiss, J. Rothman, G. Destefanis, J.-P. Chamonal, *J. Electron. Mater.* **2008**, *37*, 1261.
- [44] R. Dalven, *Infrared Phys.* **1969**, *9*, 141.
- [45] A. A. Balandin, *Nat. Nanotechnol.* **2013**, *8*, 549.
- [46] P. Dutta, P. M. Horn, *Rev. Mod. Phys.* **1981**, *53*, 497.
- [47] Y. Chen, C. M. Van Vliet, P. M. Koenraad, G. L. Larkins, *J. Appl. Phys.* **1999**, *86*, 6206.
- [48] L. Zhu, J. Huang, Z. Xie, Z. Deng, L. Chen, C. Lin, B. Chen, *IEEE Trans. Electron Devices* **2020**, *67*, 547.
- [49] A. Kerlain, A. Brunner, D. Sam-Giao, N. Pére-Laperne, L. Rubaldo, V. Destefanis, F. Rochette, C. Cervera, *J. Electron. Mater.* **2016**, *45*, 4557.
- [50] J. Chen, J. Chen, X. Li, J. He, L. Yang, J. Wang, F. Yu, Z. Zhao, C. Shen, H. Guo, G. Li, X. Chen, W. Lu, *npj Quantum Mater.* **2021**, *6*, 103.
- [51] X. Li, J. Chen, J. He, J. Chen, H. Guo, L. Yang, C. Shen, F. Yu, Z. Zhao, G. Li, X. Chen, W. Lu, *IEEE J. Sel. Top. Quantum Electron.* **2022**, *28*, 3804107.
- [52] A. Singh, R. Pal, *Solid-State Electron.* **2018**, *142*, 41.
- [53] M. Kopytko, J. Sobieski, W. Gawron, P. Martyniuk, *Sensors* **2022**, *22*, 924.
- [54] X. Sun, W. Lu, G. Yang, S. Babu, J. M. Lauenstein, A. L. e. Roch, I. Baker, presented at *Infrared Technology and Applications XLVIII Effects of proton irradiation on a SAPHIRA HgCdTe avalanche photodiode array*, Orlando, April **2022**.
- [55] A. C. Bailey, B. Yates, *Proc. Phys. Soc.* **1967**, *91*, 390.
- [56] W. D. Lawson, F. A. Smith, A. S. Young, *J. Electrochem. Soc.* **1960**, *107*, 206.
- [57] T. Xu, H. Wu, J. Si, C. Cao, *Appl. Surf. Sci.* **2007**, *253*, 5457.
- [58] B. Zhang, C. Cai, L. Hu, X. Wei, H. Wu, *Appl. Surf. Sci.* **2011**, *257*, 1986.
- [59] C. Cai, S. Jin, H. Wu, B. Zhang, L. Hu, P. J. McCann, *Appl. Phys. Lett.* **2012**, *100*, 182104.
- [60] B. Weng, J. Qiu, L. Zhao, C. Chang, Z. Shi, *Appl. Phys. Lett.* **2014**, *104*, 121111.
- [61] T. Shu, P. Lu, B. Zhang, M. Wang, L. Chen, X. Fu, G. Xu, H. Wu, *J. Cryst. Growth* **2015**, *420*, 17.
- [62] H. Zogg, K. Alchalabi, D. Zimin, K. Kellermann, *IEEE Trans. Electron Devices* **2003**, *50*, 209.
- [63] S. Goedecker, M. Teter, J. Hutter, *Phys. Rev. B* **1996**, *54*, 1703.
- [64] J. P. Perdew, K. Burke, M. Ernzerhof, *Phys. Rev. Lett.* **1996**, *77*, 3865.
- [65] H. J. Monkhorst, J. D. Pack, *Phys. Rev. B* **1976**, *13*, 5188.